RESEARCH ARTICLE

Check for updates

Structural confinement-induced highly efficient deep-red emission and negative thermal quenching performance in Mn⁴⁺-activated Ca₇Mg₂Ga₆₋ᵧAlᵧO₁₈:Mn⁴⁺ phosphors†

Jinmei Huang,[a] Pengfei Jiang, [ID] *[a] Zien Cheng,[a] Rong Wang,[b] Rihong Cong [ID] [a] and Tao Yang [ID] *[a]

High quantum efficiency (QE) and thermally stable emission are indispensable for the application of phosphors. Owing to the strong coupling between the lattice and naked d-orbitals of Mn^{4+}, Mn^{4+}-activated oxide red-emitting phosphors usually exhibit a low QE and serious thermal quenching (TQ), which strictly inhibit their prospective application. Herein, we rationally designed a novel phosphor series $Ca_7Mg_2Ga_{6-y}Al_yO_{18}:0.02Mn^{4+}$ ($CMGA_yO:Mn^{4+}$, $0 \leq y \leq 1.5$), which adopts a high structural symmetry of the space group $F432$. Highly efficient and thermally stable deep-red emissions (λ_{em} = 721 nm) were achieved simultaneously by structurally confining the Mn^{4+}-emitting centres at the isolated octahedrally coordinated sites. Specifically, the highest internal and external quantum efficiencies of 90.2 and 75.9%, respectively, were obtained for $CMGA_{1.5}O:Mn^{4+}$ due to Al^{3+}-alloying-induced local structure modification and suppression of non-radiative transitions. Excellent thermal stabilities of 99, 102.2, and 87.9% of room-temperature photoluminescence intensities were retained at 423 K for $CMGA_yO:Mn^{4+}$ with y = 0, 0.5, and 1.5, respectively. $CMGA_{0.5}O:Mn^{4+}$ exhibits an abnormal negative TQ behaviour over the measured temperature range (298–473 K), which is attributed to the energy gain *via* the electron–phonon interactions of the isolated MnO_6 octahedra. Moreover, *in situ* high-pressure emission spectra of $CMGO:0.02Mn^{4+}$ showed that the emission position is highly sensitive to the external pressure with redshift coefficients of 2.8(2) and 1.16(4) nm GPa⁻¹ in different pressure regions. These excellent photoluminescence properties of $CMGA_yO:Mn^{4+}$ phosphors signify their great application potential in red LEDs and optical pressure sensors. The findings of this work have paved an avenue for the design of high-performance Mn^{4+}-activated phosphors.

1. Introduction

Phosphor-converted white light emission diodes (pc-WLEDs) have been considered as the most promising next-generation artificial lighting source because of their attractive advantages, including low energy consumption, small size, environmental friendliness, high luminescence efficiency, and lasting durability.[1–5] The prevalent and currently commercialized method for achieving white light emission is the combination of a blue InGaN chip with the yellow phosphor $Y_3Al_5O_{12}:Ce^{3+}$ (YAG:Ce^{3+}).[6] However, the insufficient red component in the

spectrum inevitably results in a poor colour rendering index (CRI) and high correlated colour temperature (CCT), which thus stimulated the development of other rare-earth-activated red phosphors.[7] Unfortunately, these red phosphors still have several shortcomings, including the high cost of rare-earth dopants, low utilization efficiency, and incomplete colour display.[8] Moreover, red to deep-red light (620–735 nm) is also indispensable for plant growth in prompting photosynthesis, phototropism, and photomorphogenesis.[9,10] Hence, in terms of providing plants with customized light to replenish sunlight, pc-LEDs have shown overwhelming advantages of controllable illumination intensity, quality, and cycle to natural light, which is critical for improving agricultural outputs and tuning plant growth. Therefore, it is imperative to develop red phosphors that coincide with the application requirements of high-quality WLEDs and plant cultivation.

Recently, Earth-abundant and low-cost Mn^{4+}-activated red phosphors have attracted substantial attention because of the

[a]College of Chemistry and Chemical Engineering, Chongqing University, Chongqing 401131, China. E-mail: pengfeijiang@cqu.edu.cn, taoyang@cqu.edu.cn
[b]School of Metallurgy and Materials Engineering, Chongqing University of Science & Technology, Chongqing 401331, P. R. China
†Electronic supplementary information (ESI) available. See DOI: https://doi.org/10.1039/d3qi00252g

2776 | *Inorg. Chem. Front.*, 2023, **10**, 2776–2787

This journal is © the Partner Organisations 2023

intensive excitation spectrum covering the n-UV to blue light region and the red emission spanning from 600 to 780 nm.[10] Mn^{4+} ions favour an octahedrally coordinated environment and their emission wavelength is highly dependent on the covalent Mn^{4+}-ligand bonding.[11] Consequently, the Mn^{4+} ion in fluorides usually exhibits sharp line-shape red emissions, whereas Mn^{4+}-doped oxide phosphors usually give rise to broad-band red emissions due to the much stronger covalency of the $Mn^{4+}–O^{2-}$ bond than that of $Mn^{4+}–F^-$. This distinct difference in chemical bonding also makes Mn^{4+}-doped fluorides exhibit much higher quantum efficiency than Mn^{4+}-activated oxides, making Mn^{4+}-doped fluorides particularly attractive for modern-day WLEDs.[12–24] However, the moisture and high-temperature lability as well as the heavy use of toxic and corrosive HF during the synthesis process strongly restrict their widely practical application. Alternatively, Mn^{4+}-activated oxide phosphors have outstanding thermal and chemical stability and eco-friendly preparation procedures, signifying their broad prospective applications. Consequently, numerous Mn^{4+}-activated oxides, in particular B-site-ordered double perovskites, have been investigated as red-phosphors.[25–34] However, the luminescence performances of Mn^{4+} ions in oxide matrixes are significantly affected by the degree of cationic ordering, structural distortion, and defect-induced self-reduction of Mn^{4+} to Mn^{2+}, which usually results in low quantum efficiency and severe thermal quenching (TQ). Therefore, it is urgent and essential to discover novel Mn^{4+}-activated oxide phosphors exhibiting extraordinary luminescence thermal stability and extremely high efficiency.

Herein, in an attempt to explore highly efficient and thermally stable red-emitting phosphors, we rationally designed a new phosphor series $CMGA_yO:Mn^{4+}$, which has not been reported yet. The structure confinement effect led to the formation of isolated Mn^{4+}-emitters with $Mn^{4+}–Mn^{4+}$ distances >10.7 Å. These isolated Mn^{4+}-emitters exhibit highly efficient deep-red emissions (λ_{em} = 721 nm) with IEQ and EQE values of 90.2 and 75.9%, respectively, achieved by Al^{3+}-alloying. Such high quantum efficiencies reach up to the top values of hitherto documented Mn^{4+}-activated oxide phosphors. More impressively, negative TQ, which is rarely observed for Mn^{4+}-activated oxide phosphors, was also achieved by Al-alloying-induced suppression of non-radiative transitions. The findings of this research indicate that the structural confinement of isolated Mn-emitters can serve as a powerful strategy for the design of high-performance Mn^{4+}-activated oxide red phosphors.

2. Experimental section

2.1 Synthesis

Polycrystalline powder samples of $Ca_7Mg_2Ga_6O_{18}:xMn^{4+}$ (x = 0.01, 0.02, 0.03, 0.0375, 0.05, 0.0625, and 0.10) and $CMGA_yO:Mn^{4+}$ (y = 0.25, 0.5, 1.0, and 1.5) were synthesized *via* conventional high-temperature solid-state reactions. Raw materials of calcium carbonate ($CaCO_3$, Alfa Aesar, 99.99%), magnesium

oxide (MgO, Alfa Aesar, 99.99%), gallium oxide (Ga_2O_3, Alfa Aesar, 99.99%), aluminum oxide (γ-Al_2O_3, Alfa Aesar, 99.95%), and manganese oxide (MnO_2, Alfa Aesar, 99.95%) were used without further purification. First, all these reagents except for MnO_2 were dried at 500 °C for 10 h to remove the absorbed moisture before being weighed. Then, these raw materials were mixed in a stoichiometric ratio and preheated at 1000 °C to decompose the carbonates. Finally, all resulting powders were reground and pelleted and then calcinated at 1220 °C for 30 h with intermediate regrinding and re-pelleting.
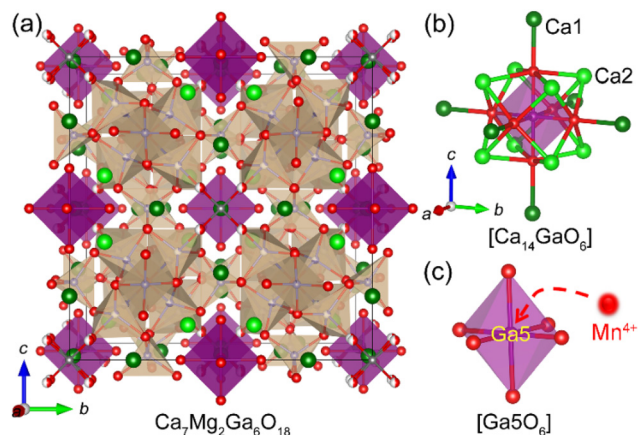
2.2 Characterization

The phase purity of the phosphors was evaluated by lab powder X-ray diffraction (PXRD) using a PANalytical Empyrean diffractometer in the Bragg–Brentano geometry with Cu K_α diffraction. The working voltage and current were 40 kV and 40 mA, respectively. High-quality PXRD data used for Rietveld refinements were collected in the 2θ-range of 5–120° with a step size of 0.0131° and a counting time of 200 s. Rietveld refinements were performed using the TOPAS-Academic V7 software.[35] Room temperature photoluminescence (PL) spectra and PL excitation (PLE) spectra for $Ca_7Mg_2Ga_6O_{18}:xMn^{4+}$ (denoted as $CMGO:xMn^{4+}$) and $Ca_7Mg_2Ga_{6-y}Al_yO_{18}:0.02Mn^{4+}$ (denoted as $CMGA_yO:Mn^{4+}$) were recorded using a Hitachi F-7100 fluorescence spectrophotometer with a solid accessory. PL decay curves, internal and external quantum efficiencies (IQE and EQE), and temperature-dependent PL spectra were recorded using an Edinburgh FLS-1000 spectrometer equipped with a 450 W continuous-wave Xe lamp and a heating system. *In situ* high-pressure spectra of $CMGA_yO:Mn^{4+}$ (y = 0 and 1.5) were recorded using a home-designed spectrometer (Ideaoptics, Shanghai, China), and the 375 nm laser source was generated from the PicoQuant LDH diode head. An asymmetrical diamond anvil cell (DAC) was employed to generate high pressure. Pre-compressed phosphors and ruby balls were loaded into the chamber. Silicone oil was employed as the pressure medium for all high-pressure measurements, and the pressure was calibrated according to the fluorescence peak at 694.2 nm of the ruby balls, excited by the 405 nm incident light. The ultraviolet-visible (UV-vis) light diffuse reflectance spectra for $CMGO:xMn^{4+}$ (x = 0.02 and 0.10) were measured at room temperature using a Shimadzu UV-3600 spectrometer operating over a wavelength from 200 to 800 nm. The fine powders were spread on compressed $BaSO_4$ as a 100% reflectance standard. The 310 nm UV-chip was purchased from Anhui UV-Chips semiconductor technology Co. Ltd. The EQE values of the deep-red pc-LED under various currents were measured using an HAAS 2000 photoelectric measuring system (EVERFINE, China).

3. Results and discussion

3.1 Crystal structure and phase identification

$Ca_7Mg_2Ga_6O_{18}$ (CMGO) crystallizes in a cubic structure described by the space group $F432$.[36] Mg^{2+} and Ga^{3+} ions

This journal is © the Partner Organisations 2023

Inorg. Chem. Front., 2023, **10**, 2776–2787 | **2777**

Fig. 1 (a) The crystal structure of CMGO viewed along the *a*-axis. (b) The surrounding environment of the Ga5O$_6$ octahedron. (c) The coordination environment of the Ga5 ion.

occupy five crystallographically independent *M*-sites (*M*1–*M*5). The tetrahedrally coordinated *M*1–*M*3 sites are co-occupied by Mg^{2+} and Ga^{3+} cations, while the remaining 4-fold coordinated *M*4 and 6-fold coordinated *M*5 (Ga5) sites are occupied exclusively by Ga^{3+} ions. As shown in Fig. 1, the structural framework of CMGO is built by MO_4-tetrahedra through corner-sharing, leaving the large voids distributed over the body and edge centres of the unit cell. These structural cavities are stuffed by the $[Ca_{14}GaO_6]$ cluster, which is composed of six Ca1 cations and a perovskite-like $[CaGaO_3]$ unit with a regular $Ga5O_6$ octahedron (Fig. 1b and c). The isolated $Ga5O_6$ octahedrons in the CMGO matrix are well separated from each other with a minimum distance of ~10.7 Å. Such a structural feature of CMGO coincides with our target design of high-performance Mn^{4+}-activated oxide phosphors, which thus promoted us to investigate the photoluminescence of CMGO: Mn^{4+}.

PXRD patterns of CMGA$_y$O:Mn^{4+} and CMGO:xMn^{4+} phosphors are shown in Fig. 2a and S1,† respectively. PXRD patterns of these phosphors show similar profiles and are consist-
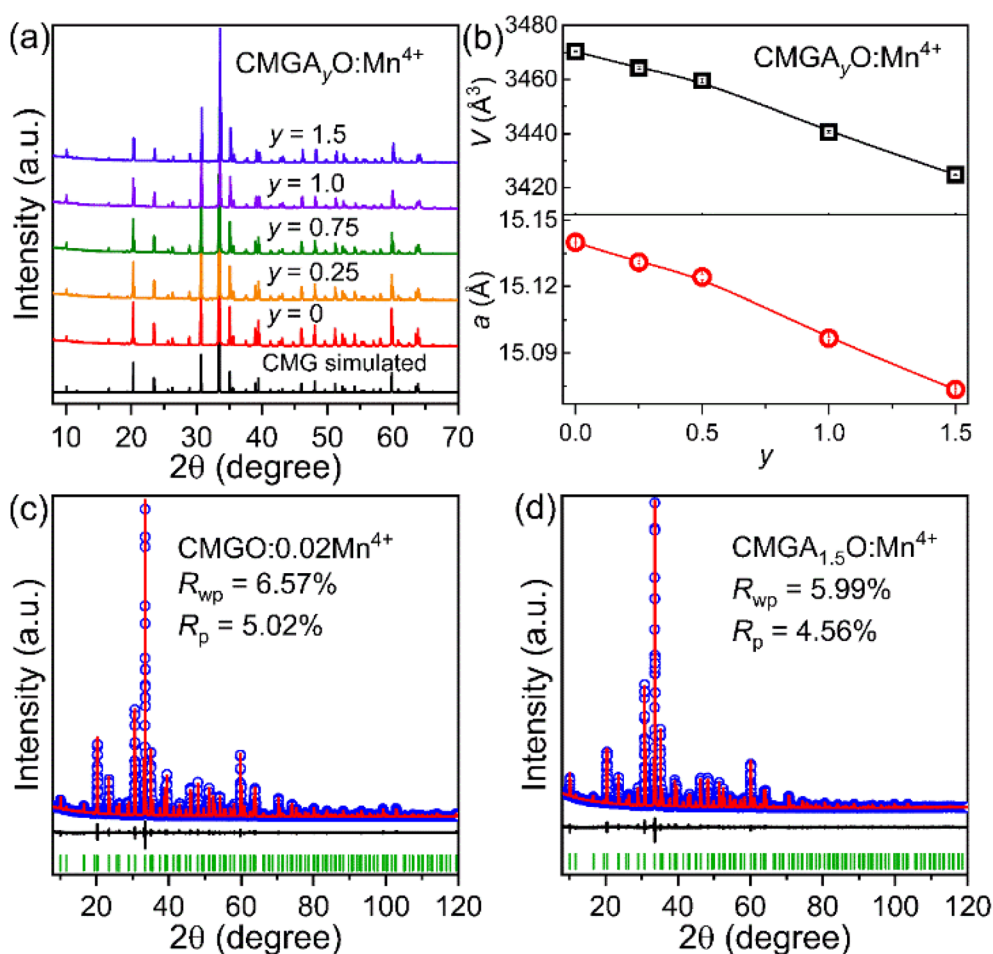
Fig. 2 (a) PXRD patterns for CMGA$_y$O:Mn^{4+}. (b) Plots of lattice parameters and cell volumes as a function of the Al^{3+}-content (*y*) in CMGA$_y$O:Mn^{4+}. Rietveld refinement plots of PXRD data for CMGO:0.02Mn^{4+} (c) and CMGA$_{1.5}$O:Mn^{4+} (d). The blue circles and red and black solid lines represent the observed, calculated, and differences between the former two, respectively. The expected Bragg positions are given as green bars at the bottom of the patterns.

ent with that of the pristine CMGO host, indicating all these materials are phase-pure and isomorphous. The lattice parameters of CMGO:xMn^{4+} are independent of chemical compositions (Fig. S2†), suggesting that the incorporation of Mn^{4+} has a negligible impact on the crystal structure. In contrast, the equivalent substitution of Ga^{3+} ions (0.62 Å in 6-fold coordination) with smaller Al^{3+} (0.535 Å in 6-fold coordination) ions in CMGA$_y$O:Mn^{4+} led to progressive peak shifts toward high-angle regions (Fig. 2a).[37] This observation is in line with the linear decreases of lattice parameters as a function of the Al^{3+}-content (y) (Fig. 2b), firmly corroborating that Al^{3+} ions were successfully incorporated into the host lattice. We should note that the solution range of Al^{3+} in CMGA$_y$O:Mn^{4+} is limited to $y \leq 1.5$ because a higher Al^{3+}-doping content led to the formation of the impurity phase Ca$_3$Al$_2$O$_6$ (Fig. S3†). To further shed light on the Al^{3+}-substitution-induced structural modifications, Rietveld refinements were performed on CMGA$_y$O:Mn^{4+} ($y \leq 1.5$). Since Mg^{2+} and Al^{3+} cations possess identical X-ray scattering abilities, they were regarded as the same cation during the refinement process. The PXRD data for CMGA$_y$O:Mn^{4+} were perfectly fitted using CMGO as the initial structure model. The final Rietveld refinement patterns are shown in Fig. 2c and d and S4.† As shown in Fig. S5,† all the refined average M–O bond lengths in CMGA$_y$O:Mn^{4+} show apparent contraction trends, involving a noticeable contraction of the M3–O bond length and slight contractions of the remaining M–O bond lengths, indicating that Al^{3+} ions tend to reside on the tetrahedrally coordinated M3-site.

3.2 Photoluminescence properties of CMGO:xMn^{4+}

PLE spectra (λ_{em} = 721 nm) of CMGO:xMn^{4+} phosphors comprise two absorption bands spanning from 250 to 550 nm (Fig. 3a and S6†), signifying that these phosphors can be excited by both ultraviolet and blue LED chips. These two absorption bands are consistent with the broad absorption bands centred at 305 and 465 nm in the UV-vis light reflectance spectra of CMGO:xMn^{4+} (x = 0.02 and 0.10) (Fig. S7†). The PLE spectrum of CMGO:0.02Mn^{4+} can be well deconvolved into four Gaussian peaks centred at ~280 (~35 715 cm^{-1}), 303 (~33 003 cm^{-1}), 338 (~29 586 cm^{-1}), and 464 nm (~21 552 cm^{-1}), corresponding to the contributions of O^{2-}-to-Mn^{4+} charge transfer (CT) and ^{4}A$_{2g}$ → ^{4}T$_{1g}$, ^{4}A$_{2g}$ → ^{2}T$_{2g}$, and ^{4}A$_{2g}$ → ^{4}T$_{2g}$ transitions of Mn^{4+} ions, respectively.[11,38]

Upon excitation at 291 nm, CMGO:xMn^{4+} phosphors emit bright red light in the wavelength range of 660–780 nm, which is ascribed to the spin-forbidden ^{2}E$_g$ → ^{4}A$_{2g}$ transition of the Mn^{4+} ion. As illustrated in Fig. 3b and c, the emission intensity first increases along with the doping content (x) of Mn^{4+} ions and reaches a maximum at x = 0.02 and then declines gradually due to the onset of concentration quenching. Importantly, although Mn^{4+}-activators in CMGO:Mn^{4+} experience a similar surrounding environment to those in perovskites (Fig. 1b), the optimal doping content (x = 0.02) is much higher than those of the Mn^{4+}-activated perovskite-type phosphors (see Table 1). It is vitally important for the application of Mn^{4+}-doped materials in w-LEDs and pc-LEDs, as high Mn^{4+} doping con-

centrations are required for sufficient absorption of the blue LED light in parity-forbidden Mn^{4+} d–d transitions. Together with the crystal structure features, we can speculate that the structural confinement of Mn^{4+} activators at isolated octahedral sites can effectively inhibit the energy migration amongst the Mn^{4+} ions, which is critical for the achievement of high-concentration Mn^{4+} doping. Impressively, the IQE and EQE values for CMGO:0.02Mn^{4+} were estimated to be 85.2% and 66.1%, respectively (Fig. S8†). These values are superior to most of the Mn^{4+}-activated oxide phosphors tabulated in Table 1.

Intriguingly PL spectra of CMGO:xMn^{4+} comprise a periodic peak series with an energy interval of ~25 meV, which differs dramatically from most of the Mn^{4+}-activated oxide phosphors. Such a spectroscopic feature was previously observed for a limited number of Mn^{4+}-activated phosphors, including Ca$_3$ZnAl$_4$O$_{10}$:Mn^{4+},[39] Ca$_{14}$Zn$_6$(Al/Ga)$_{10}$O$_{35}$:Mn^{4+},[40] La$_2$LiTaO$_6$:Mn^{4+},[41] and La$_2$MgTiO$_6$:Mn^{4+}.[42] To shed light on this spectroscopic feature, low-temperature PL spectra for CMGO:0.02Mn^{4+} were collected in the temperature range of 10–250 K. As seen in Fig. S9,† the intensity of the peak sideband at the high energy side (<700 nm) decreases upon cooling and disappears completely at 10 K. In contrast, the sideband at the low energy side (>700 nm) increases sharply with decreasing temperature. These spectroscopic features of Mn^{4+}-emitters suggest that the emission peak at ~700 nm is ascribed to the zero phonon line (ZPL) of the spin-forbidden ^{2}E$_g$ → ^{4}A$_{2g}$ transition, the low energy (>700 nm) and high energy (<700 nm) sidebands are assigned to be the phonon-associated Stokes and anti-Stokes shift emission peaks, respectively.

The well-known Tanabe–Sugano energy level diagram was further illustrated to understand the deep-red emissions for Mn^{4+}-emitters in CMGO in-depth. As shown in Fig. 3d, the ZPL excitation and emission energies are related to the crystal field strength D_q and Racah parameters B and C. Based on the ZPL energy levels of ^{4}T$_{2g}$, ^{4}T$_{1g}$, and ^{2}E$_g$ states, the values of D_q, B, and C can be estimated using the following equations:[8,38]

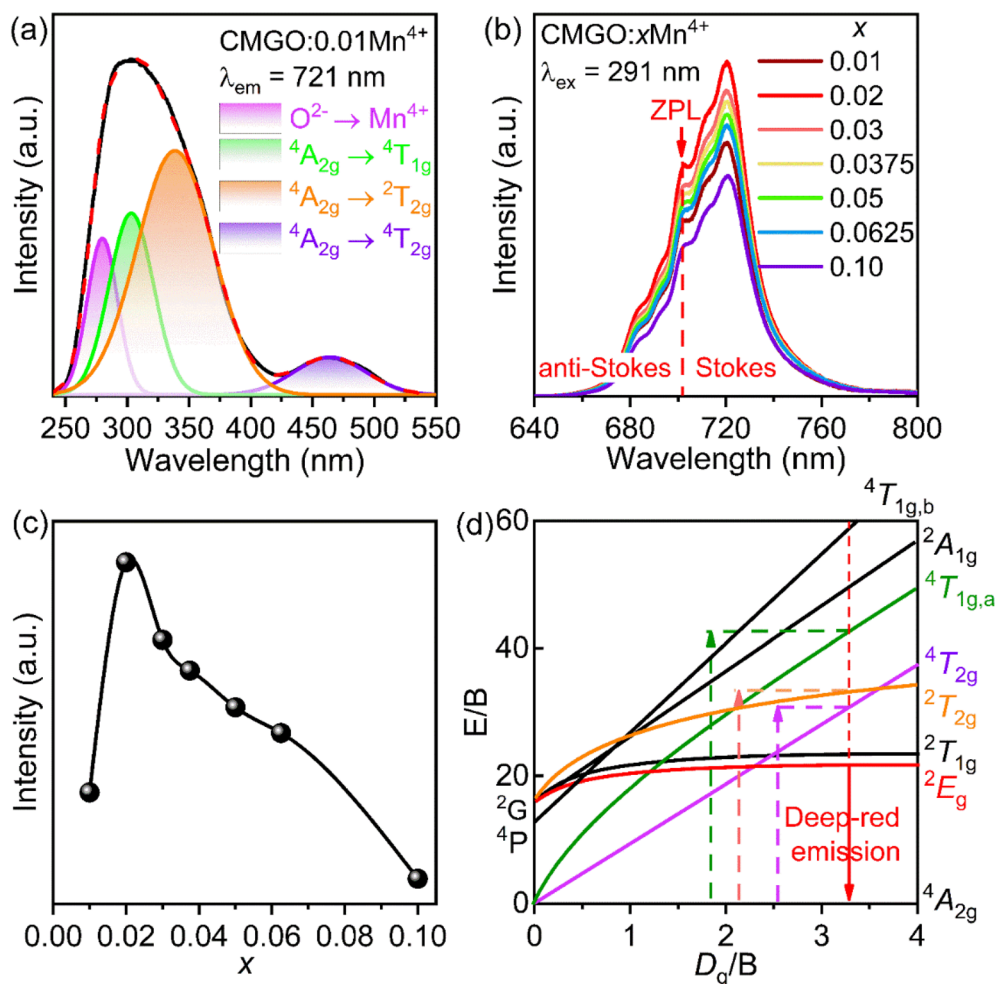$$10D_q = E(^4\text{T}_{2g} \rightarrow {}^4\text{A}_{2g}) \tag{1}$$

$$D_q/B = 15(\delta - 8)/(\delta^2 - 10\delta) \tag{2}$$

$$\delta = \frac{E(^4\text{A}_{2g} \rightarrow {}^4\text{T}_{1g}) - E(^4\text{A}_{2g} \rightarrow {}^4\text{T}_{2g})}{D_q} \tag{3}$$

$$\frac{E(^2\text{E}_g \rightarrow {}^4\text{A}_{2g})}{B} = \frac{3.05C}{B} - \frac{1.8B}{D_q} + 7.9 \tag{4}$$

The values of the D_q, B, and C were calculated as 2155, 842, and 2561 cm^{-1}, respectively. Then the D_q/B value was calculated as 2.56, corresponding to a ^{2}E$_g$/B (E/B) value of 21.7 (see Fig. 3d). However, such a crystal field strength would lead to a ZPL emission energy of 18 270 cm^{-1} (547 nm) for the ^{2}E$_g$ → ^{4}A$_{2g}$ transition according to the expression $E(^2\text{E}_g \rightarrow {}^4\text{A}_{2g})_{ZPL}$ = 21.7B, contradicting the detected ZPL emission energy of 14 245 cm^{-1} (702 nm). Such a large discrepancy has been fre-

This journal is © the Partner Organisations 2023

Inorg. Chem. Front., 2023, **10**, 2776–2787 | **2779**

Fig. 3 (a) The excitation spectrum of CMGO:0.01Mn^{4+}. (b) The PL spectra for CMGO:xMn^{4+}. (c) The evolution of integrated PL intensities of CMGO: xMn^{4+} as a function of the Mn^{4+}-content (x). The inset shows the linear fitting of the lg(I/x) − lg(x) curve. (d) The Tanabe–Sugano energy level diagram of Mn^{4+} (d^3) in the octahedral crystal field of the CMGO host.

Table 1 Comparison of photoluminescence of some excellent Mn^{4+}-activated far-red phosphors

Host matrix	Mn^{4+}-content	λ_{em} (nm)	IQE (%)	EQE (%)	Intensity (%, 150 °C)	Ref.
CaGdAlO$_4$	0.002	713	61	—	—	47
CaNa$_{0.5}$La$_{0.5}$MgWO$_6$	0.009	700	94	82	—	31
Ca$_3$La$_2$W$_2$O$_{12}$	0.016	711	48	—	29	48
Ca$_3$Al$_4$ZnO$_{10}$	0.016	714	60	—	51	39
NaMgLaTeO$_6$	0.02	703	57.4	—	75	32
Gd$_2$ZnTiO$_6$	0.002	705	65.6	39.7	27	30
La$_2$LiSbO$_6$	0.003	712	92	—	58	49
La$_{1-x}$Lu$_x$AlO$_3$	0.001	729	86	62.1	<20	50
CMGO	0.02	721	85.2	66.1	99	This work
CMGA$_{1.5}$O	0.02	721	90.2	75.9	87.9	This work

quently encountered for Mn^{4+}-activated phosphors and stems from the use of the peak energies of PL and PLE bands rather than their ZPL energies in the calculations of eqn (1)–(4). Additionally, the ZPL energies of PLE states are barely determined accurately, particularly for $E(^4T_{1g})_{ZPL}$, which is the critical issue that leads to unreliable Racah parameters.

Recently, Adachi proposed a revised model to estimate more accurate values of the Racah parameters based on the standard crystal-field theory.[43–45] The most important assumption of the revised model is that the Racah parameters exhibit a quantitative relationship of $C = 4.7B$.[43–45] In combination with eqn (1) and (4), the values of B and C parameters were

revised as 657 and 3088 cm^{-1}, respectively. The D_q/B value was then calculated as 3.28, implying Mn^{4+} experiences a strong crystal field strength. Furthermore, the expected ZPL emission wavelength was further derived to be 701 nm (14 257 cm^{-1}), which matches well with the measured ZPL emission wavelength (702 nm) of CMGO:xMn^{4+}. Therefore, the revised Racah and crystal field parameters are self-affirming, strongly confirming the validation of these parameters.

It is known that the emission of the Mn^{4+} ion is in fact determined by the strength of the Mn^{4+}-ligand covalent bonding, namely the nephelauxetic effect (β_1), which can be quantified according to the following equation:[46]

$$\beta_1 = \sqrt{\left(\frac{B}{B_0}\right)^2 + \left(\frac{C}{C_0}\right)^2} \qquad (5)$$

Where B_0 (1160 cm^{-1}) and C_0 (4303 cm^{-1}) are Racah parameters for a free Mn^{4+} ion. A smaller β_1 value indicates a stronger covalent Mn^{4+}-ligand bonding, thus resulting in a longer emission wavelength. Herein, the value of β_1 was calculated to be 0.91, indicating a strong covalent Mn^{4+}–O^{2-} bonding in CMGO. Quantitatively, for most Mn^{4+}-activated oxide phosphors, the energy of the $^2E_g \rightarrow {}^4A_{2g}$ transition can be further predicted using the β_1-related linear equation:[46]

$$E(^2E_g \rightarrow {}^4A_{2g}) = -880.49 + 16\,261.92\beta_1 \pm \sigma \qquad (6)$$

where σ represents the root-mean-square deviation with a value of 332 cm^{-1}. According to the β_1 value, the emission energy of $E(^2E_g \rightarrow {}^4A_{2g})$ for CMGO:Mn^{4+} is expected in the range of 13 586–14 250 cm^{-1}. According to the PL spectra of CMGO:Mn^{4+}, the value of $E(^2E_g \rightarrow {}^4A_{2g})$ is calculated as 14 225 cm^{-1}, within the predicted energy range, thereby explaining the deep-red emission of the Mn^{4+} ion in CMGO: Mn^{4+}.

3.3 Al-alloying-induced significantly improved photoluminescence properties

Chemical substitution is widely utilized to manipulate the local structure of Mn^{4+}-activators, so as to the realize efficient red-emission. Our attempt of equivalent Al^{3+}-to-Ga^{3+} substitution in CMGA$_y$O:Mn^{4+} was applied to improve the photoluminescence performance. As shown in Fig. 4a, PL intensities were enhanced expectedly by incorporating Al^{3+} ions into CMGA$_y$O:Mn^{4+}. Quantum efficiency measurements further revealed that both the IQE and EQE values were improved remarkably from 85.2 and 66.1% for $y = 0$ to 90.2 and 75.9% for $y = 1.5$ (Fig. 4b and S8†), reaching up to the top values of previously reported Mn^{4+}-activated oxide phosphors. As seen in Fig. 4c, the decay curves for CMGA$_y$O:Mn^{4+} monitored at 721 nm were perfectly fitted with a single exponent function given below:

$$I(t) = I_0 A \exp\left(-\frac{t}{\tau}\right) \qquad (7)$$

where $I(t)$ and I_0 are the intensities at time t and 0, respectively, A is a constant, and τ is the decay time. These results demonstrate that there exists only one type of Mn^{4+}-emitting centre in CMGA$_y$O:Mn^{4+}, which is consistent with the structural feature of the host matrix. The lifetimes were calculated to be 2.94, 2.93, 2.95, 3.03, and 3.09 ms for $y = 0$, 0.25, 0.5, 1, and 1.5 in CMGA$_y$O:Mn^{4+}, respectively. These values are comparable to previously reported millisecond scale lifetimes for Mn^{4+}-activated deep-red phosphors.[51,52] Clearly, the lifetimes of Mn^{4+} ions were prolonged by Al-alloying. According to the results of our structure analysis (Fig. S5†), Al^{3+}-alloying led to a more compact MnO$_6$-octahedron, which thus facilitated the mix of the odd parity $^4T_{2u}$ and $^4T_{1u}$ states with the even parity ^2E_g state, thereby breaking the selection rule of the spin- and parity-forbidden $^2E_g \rightarrow {}^4A_{2g}$ transitions of Mn^{4+} ions.[53]
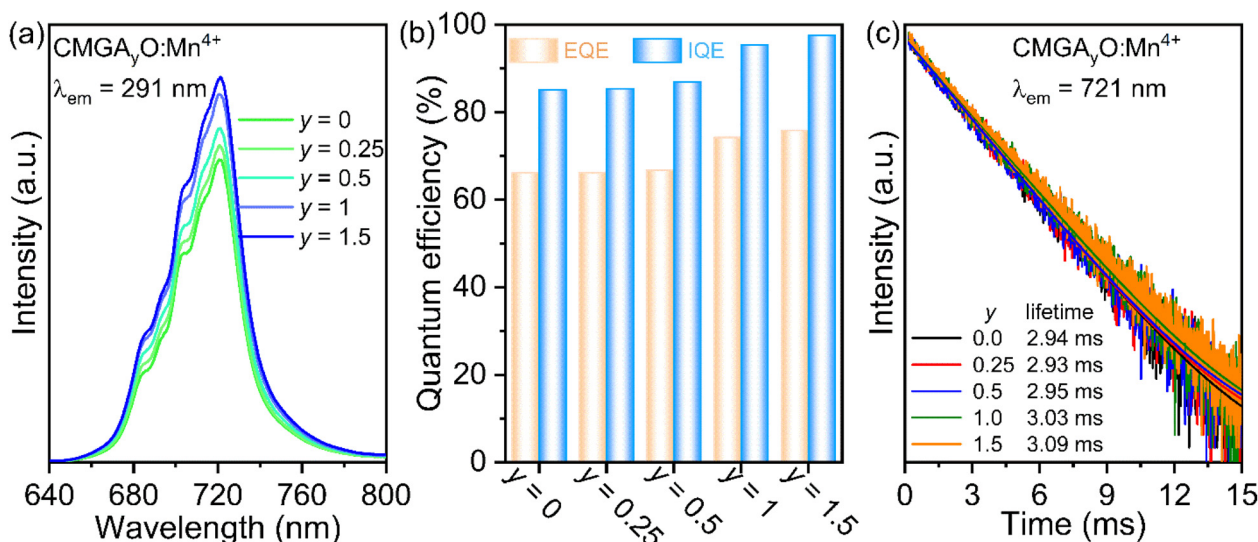

Fig. 4 PL spectra (a), internal quantum efficiencies (b), and time-resolved decay curves (c) of CMGA$_y$O:Mn^{4+}.

Additionally, the lattice contraction also consolidates the structural rigidity and thus suppresses nonradiative transition. As a result, highly efficient emission was achieved by substituting Ga^{3+} ions with smaller Al^{3+} ions in $CMGA_yO:Mn^{4+}$.

3.4 Temperature dependence of the Mn^{4+} luminescence

Besides QE, the thermal stability is another critical factor that determines the potential application of a phosphor, because the working temperature of typical LEDs can reach 150 °C (423 K). This stimulated us to further investigate the temperature-dependent PL properties of $CMGO:Mn^{4+}$ and $CMGA_yO:Mn^{4+}$ phosphors. As shown in Fig. 5a, the ZPL and Stokes vibronic emissions of $CMGO:0.02Mn^{4+}$ decline gradually upon heating, whereas the anti-Stokes vibronic emission increases along with the temperature. As a result, the integrated PL intensity first increases and reaches a maximum value at 333 K and then declines slowly. As for $CMGO:0.05Mn^{4+}$ (Fig. S10†),

all the emission peaks increase along with temperature and reach a maximum at 373 K. Then, decreases were observed for the ZPL and Stokes vibronic emissions, while the anti-Stokes emission remains an increasing trend. Consequently, $CMGO:0.05Mn^{4+}$ exhibits a wider negative TQ temperature range (298–473 K) than that of $CMGO:0.02Mn^{4+}$ (298–333 K). Impressively, as we can see in Fig. 5b, the PL intensities for $CMGO:xMn^{4+}$ with $x = 0.02$ and 0.05 at 423 K were still retained 99% and 103% of the initial intensities at 298 and 283 K, respectively, signifying their superior thermal stability to the Mn^{4+}-activated red phosphors reported so far. Moreover, the emission-peak position of $CMGO:xMn^{4+}$ is independent of the temperature, indicating outstanding color stabilities of these phosphors at high temperatures.

The effect of Al^{3+}-alloying on the PL thermal stability of $CMGA_yO:Mn^{4+}$ ($y = 0.5$ and 1.5) were also investigated and their temperature-dependent PL spectra are depicted in Fig. 5c
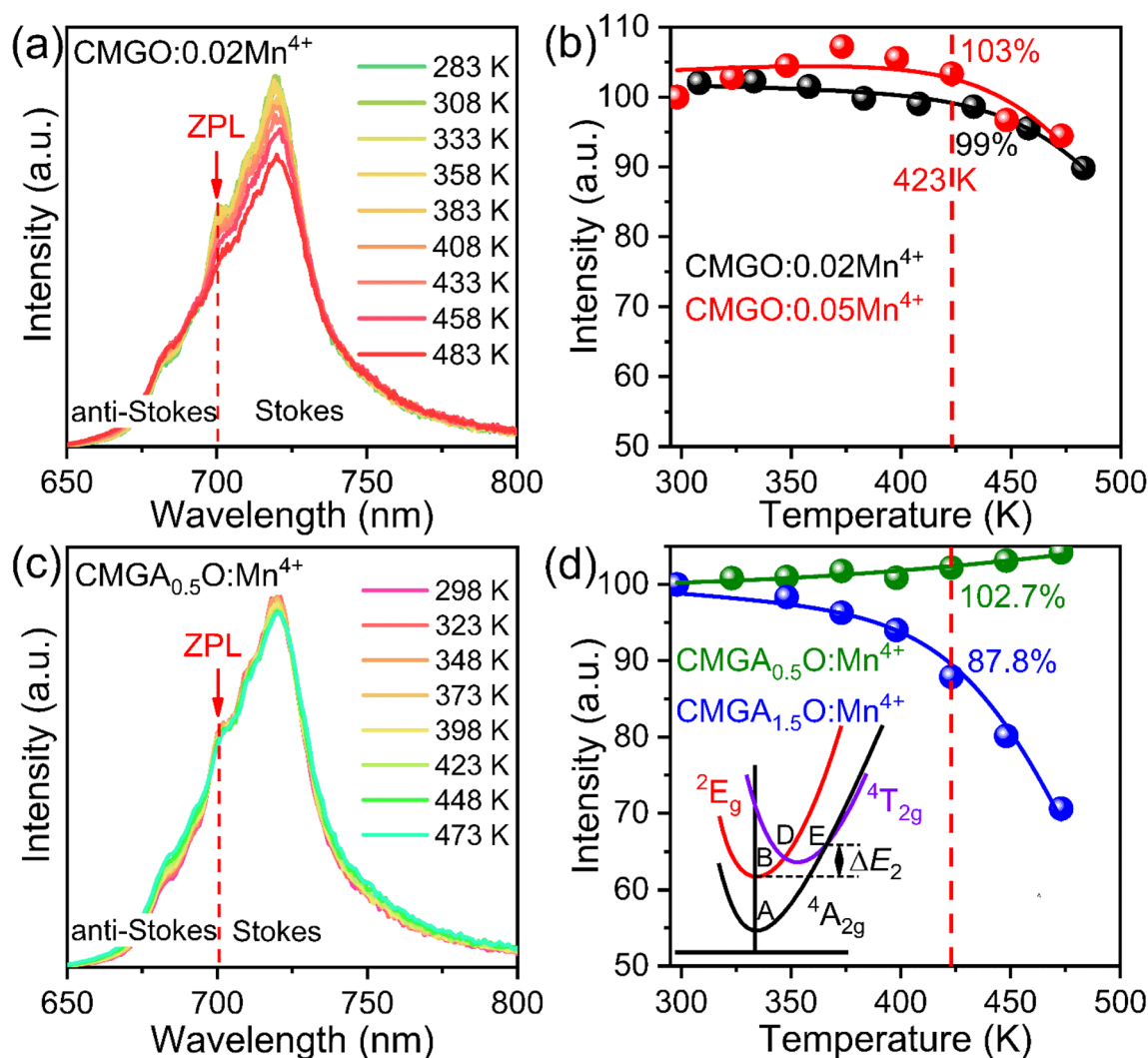
Fig. 5 Temperature-dependent PL spectra for $CMGO:0.02Mn^{4+}$ (a) and $CMGA_{0.5}O:Mn^{4+}$ (c). The evolutions of integrated PL intensity of $CMGO:xMn^{4+}$ with $x = 0.02$ and 0.05 (b) and $CMGA_yO:Mn^{4+}$ with $y = 0.5$ and 1.5 (d) *versus* temperature (T). The solid lines in (b) and (d) were obtained by fitting the $I_{PL} − T$ curves according to eqn (8). The inset of (d) shows the mechanism of TQ at high temperatures.

**2782** | *Inorg. Chem. Front.*, 2023, **10**, 2776–2787

This journal is © the Partner Organisations 2023

and S11.† The evolution of PL spectra for $CMGA_{0.5}O:Mn^{4+}$ *versus* temperature is similar to that of $CMGO:Mn^{4+}$. However, the decline trends of the ZPL and Stokes emissions of $CMGA_{0.5}O:Mn^{4+}$ were much slower, while the enhancement in anti-Stokes emissions was more significant upon heating. As a result, an abnormal negative TQ behaviour over the measured temperature range was observed for $CMGA_{0.5}O:Mn^{4+}$ (Fig. 5c) and the integrated PL intensity was enhanced to 104.2% at 473 K. In contrast to $CMGA_{0.5}O:Mn^{4+}$, sharp reductions in PL intensities of ZPL and Stokes emissions were observed for $CMGA_{1.5}O:Mn^{4+}$ at elevated temperatures. As a result, a normal TQ behaviour above room temperature was observed (Fig. S11†). However, $CMGA_{1.5}O:Mn^{4+}$ still exhibited a superior thermal stability with 87.9% with the PL intensity being retained at 423 K.

Till now, negative TQ has been observed for many Mn^{4+}-activated fluoride and oxyfluoride phosphors.[54] In contrast, a negative TQ was relatively rarely observed for Mn^{4+}-doped oxide phosphors and only a few examples have been documented as far as we know, such as $Sr_2Ca_{0.9}La_{0.1}WO_6:Mn^{4+}$[55] and $Ba_2CaWO_6:Mn^{4+}$.[56] Negative TQ observed for rare-earth-,[57,58] Bi^{3+}-,[59] and Mn^{2+}-activated[60,61] phosphors are usually attributed to the energy compensation stemming from energy transfer from the lattice defects to the emitting centres at elevated temperatures. However, recent studies on Mn^{4+}-doped fluorides have unravelled that the negative TQ is caused by an intrinsic effect, *i.e.* the electron–phonon interaction, rather than any extrinsic effects.[62] Specifically, the electric dipole (parity) forbidden Mn^{4+} $^4A_{2g} \rightarrow {}^4T_{2g}$ can gain intensity at high temperatures *via* coupling with local vibrations of the Mn^{4+}-octahedron,[63] which is the origin of negative TQ for Mn^{4+} emitters. According to Adachi, the temperature-dependent PL intensity can be quantitatively accounted for by the expression given below[63,64]

$$I_{PL}(T) = I_0 \left[1 + \frac{2}{\exp\left(\frac{h\nu_s}{k_B T}\right) - 1} \right] \times \frac{1}{1 + \sum\limits_{j}^{2} a_j \exp\left(-\frac{\Delta E_j}{k_B T}\right)} \quad (8)$$

where the term on the right side contains ν_s reflects the effective electron–phonon interactions arising from both the $^4T_{2g}$ and ^2E_g states, k_B is the Boltzmann constant. ΔE_1 ($j = 1$) and ΔE_2 ($j = 1$) represent the thermal quenching energy barriers at lower and higher temperature ranges, respectively. As shown in Fig. 5b and d, the experimental data were successively described by eqn (8). The $h\nu_s$ values for $CMGO:0.02Mn^{4+}$, $CMGO:0.05Mn^{4+}$, $CMA_{0.5}GO:Mn^{4+}$, and $CMA_{1.5}GO:Mn^{4+}$ were estimated as 73.5, 73.8, 73.8, and 73.6 eV, respectively, suggesting similar strengths of electron–phonon interactions in these phosphors due to the structural confinement effect. As shown in Table S1,† our fitting results deciphered that the negative TQ was dedicated by the a_1 value, which reflects the nonradiative combination centre density. A smaller a_1 value would thus lead to a stronger negative TQ, which matches well our experimental and fitting results (Fig. 5 and Table S1†). Despite the ΔE_1 value being of the same order of magnitude as $h\nu_s$, however, ΔE_1 is related not to the electron–phonon interaction, but to the bulk or surface defects that act as nonradiative combination centres. ΔE_2 is much larger than ΔE_1 because ΔE_2 represents the TQ energy barrier of the nonradiative relaxation process *via* the crossing point of $^4T_{2g}$ and $^4A_{2g}$ parabolas (B → C → D → A), as illustrated in the inset of Fig. 5d. The ΔE_2 values of $CMGO:0.02Mn^{4+}$,
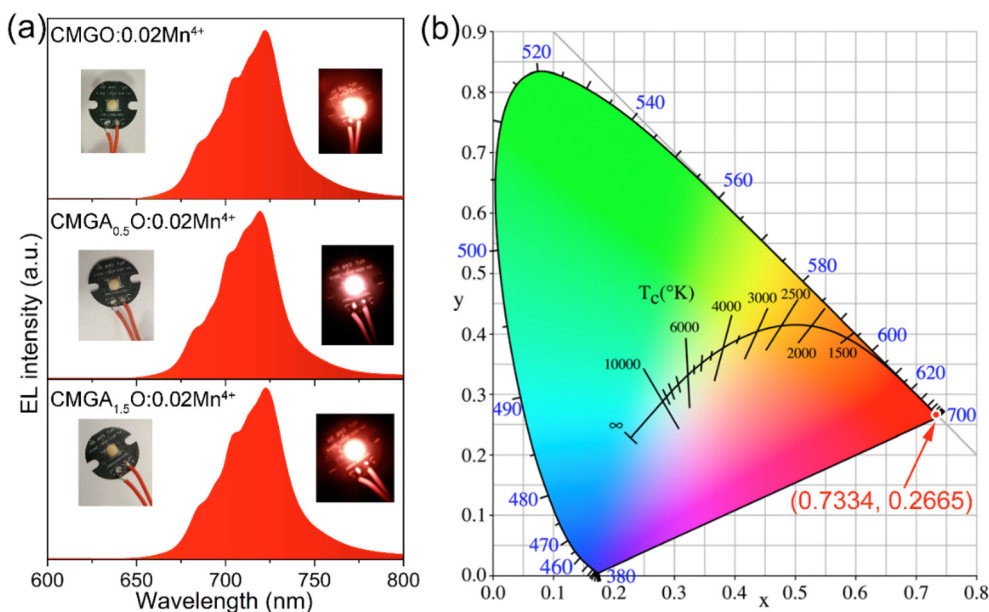
Fig. 6 (a) EL spectra of the red LED devices driven by 310 nm chips under a bias voltage of 6 V. (b) The CIE colour coordinates of electroluminescence spectra of the red LEDs.

This journal is © the Partner Organisations 2023

Inorg. Chem. Front., 2023, **10**, 2776–2787 | **2783**

CMGO:0.05Mn^{4+}, and CMA$_{1.5}$GO:Mn^{4+} were fitted to be 0.66, 0.63, and 0.59 eV, respectively. Such large ΔE_2 values successfully explain the superior thermal stabilities of these phosphors. We should also note that the ΔE_2 value of CMA$_{0.5}$GO:Mn^{4+} is inestimable because no TQ was detected at high temperatures.

3.5 Electroluminescence performance of the prepared LED devices

As discussed above, the excellent photoluminesce of CMGA$_y$O:Mn^{4+} suggests their potential applications in red pc-LEDs. CMGA$_y$O:Mn^{4+} (y = 0, 0.5, and 1.5) phosphors were thus combined with 310 nm chips to prepare the red LEDs to further evaluate their available applications. The electroluminescence (EL) spectra of the prepared red LED devices are shown in Fig. 6a. The photographs of these pc-LEDs are given in the insets of Fig. 6a, where the bright red emission light can be observed by the naked eye. Fig. 6b shows the CIE chromaticity coordinates of (0.7334, 0.2665) for the EL spectra of the fabricated red LEDs. To further demonstrate the potential applications, the electroluminescence spectra of the representative pc-LED device prepared by CMGA$_{1.5}$O:Mn^{4+} were recorded under various currents (140–300 mA). As shown in Fig. S12a,† the deep-red emission band increases along with the driven current and no saturation can be observed. The corresponding EQE value first increases along with the driven current and reaches a maxim value approaching 0.8% at 190 mA and then decreases thereafter (Fig. S12b†). The low EQE value could be further improved by optimizing the deep-red pc-LED packing procedure, which is worth exploring.

3.6 *In situ* high-pressure photoluminescence of CMGA$_y$O:Mn^{4+} (y = 0 and 1.5)

In situ pressure-dependent PL spectra of CMGO:0.02Mn^{4+} and CMGA$_{1.5}$O:Mn^{4+} were recorded over the pressure range of 0.5 to 20.2 GPa under a constant excitation wavelength of 375 nm. Upon compression, a sharp decline in the emission intensity can be observed for both CMGO:0.02Mn^{4+} and CMGA$_{1.5}$O:Mn^{4+} when the pressure is lower than 5 GPa (Fig. 7 and S13†), beyond which the emission intensity decreases slowly. When the external pressure excess is 15 GPa, the deep-red emission of CMGA$_{1.5}$O:Mn^{4+} almost completely disappeared (Fig. S13†), whereas the deep-red emission still could be detected for CMGO:0.02Mn^{4+} up to 20.2 GPa. This phenomenon might be ascribed to the pressure quenching effect because the cell volume of CMGA$_{1.5}$O:Mn^{4+} is much smaller than that of CMGO:0.02Mn^{4+}.

The Mn–O covalent bonding can be consolidated upon compression, thereby leading to a shift of the deep-red emission band toward a longer wavelength (Fig. 7 and S13†). As for CMGA$_{1.5}$O:Mn^{4+}, a red-shift of 12 nm can be obtained from 0.5 to 15 GPa with the peak shape remaining unchanged. For CMGO:0.02Mn^{4+}, a redshift of 12 nm was observed from 0.5 to 5 GPa with the emission band being dominated by the stokes sideband (insets of Fig. 7), while the ZPL emission starts to dictate the emission band and shows a 16 nm red-shift from 6.7 to 20.2 GPa, signifying a plausible structure phase tran-
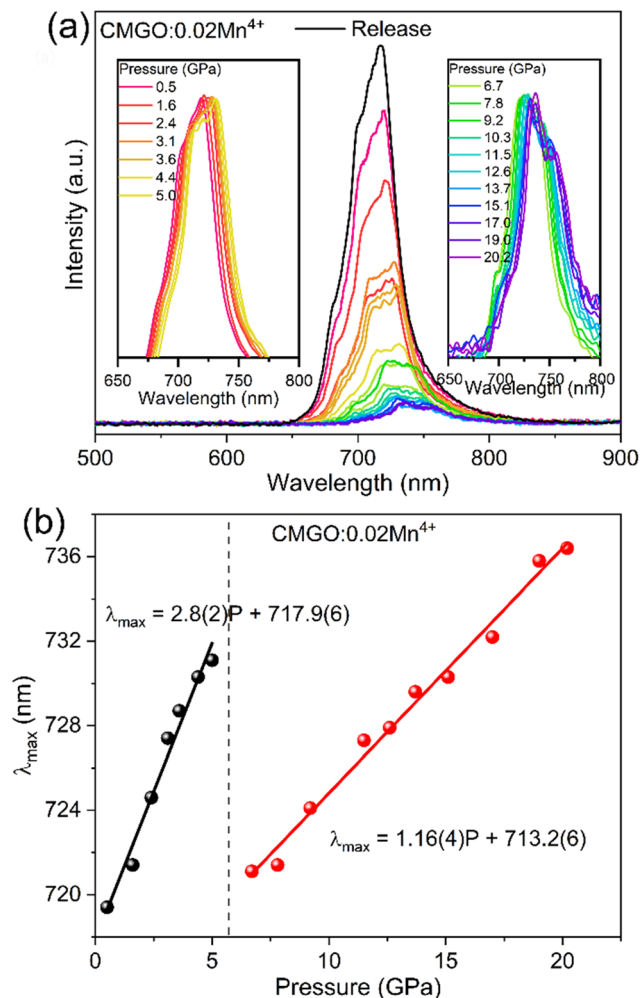

Fig. 7 (a) The emission spectra of CMGO:0.02Mn^{4+} under an excitation wavelength of 375 nm and different pressures. (b) The plots of λ_{max} as a function of pressure.

sition at around 6 GPa. Furthermore, *in situ* high-pressure PXRD should be conducted to verify this possible structure transition. This spectroscopic phenomenon reflects that Al^{3+}-alloying can consolidate the structural stiffness, which is consistent with the photoluminescence properties of CMGA$_y$O:Mn^{4+}. Upon decompression, both the emission peak position and shape can recover to the ambient state. Such a pressure-sensitive red-shift can be utilized to gauge pressure for high-pressure technology. Consequently, we plotted the wavelength at the maximal intensity (λ_{max}) as a function of pressure (P). As shown in Fig. 7b, the $\lambda_{max} - P$ curves show simple linear correlations in two distinct pressure regions. Linear fittings to the $\lambda_{max} - P$ curves resulted in pressure-sensing coefficients of 2.8(2) and 1.16(4) nm GPa^{-1} in the relatively low (0.5–5 GPa) and high (6.7–20.2 GPa) pressure-regions, respectively. We should emphasise that these pressure-sensing coefficients are much larger than those of LiCaY$_5$(BO$_3$)$_6$:Ce^{3+} and ruby (~0.35 nm GPa^{-1}, Al$_2$O$_3$:Cr^{3+}),[65,66] signifying great potential as a pressure sensor.

2784 | *Inorg. Chem. Front.*, 2023, **10**, 2776–2787

This journal is © the Partner Organisations 2023

4 Conclusion

In summary, a series of highly efficient and thermally stable far-red emission (λ_{em} = 721 nm) phosphors were rationally designed by structural confinement of Mn^{4+} ions at the octahedrally coordinated sites of the oxide host matrix CMGO. Excellent quantum efficiencies (IQE = 85.2%, EQE = 66.1%) were obtained expectedly for the CMGO:0.02Mn^{4+}. Al^{3+}-to-Ga^{3+} substitution in $CMGA_yO:Mn^{4+}$ further improved the IQE and EQE values to 90.2 and 75.9%, respectively, due to the local structural modification-induced suppression of nonradiative transitions and breaking of the selection rule of the spin- and parity-forbidden $^2E_g \rightarrow {}^4A_{2g}$ transitions of Mn^{4+} ions. This local structure modification could also facilitate the energy capture of $^2E_g \rightarrow {}^4A_{2g}$ transitions by coupling with local MnO_6-octahedral vibrations, which led to an abnormal negative thermal quenching behaviour for $CMGA_{0.5}O:Mn^{4+}$. Additionally, *in situ* high-pressure photoluminescence measurements revealed that the deep-red emission of CMGO:0.02Mn^{4+} can maintain up to a pressure as high as 20.2 GPa. More importantly, the linear positive correlations between the maximal emission wavelengths and applied pressures in two distinct pressure regions can be utilized to pressure gauge. These newly discovered phosphors exhibit superior photoluminescence to most of the previously reported Mn^{4+}-activated oxide phosphors, signifying their great potential application as far-red emission phosphors.

Conflicts of interest

The authors declare no competing financial interest.

Acknowledgements

References

1 E. F. Schubert and J. K. Kim, Solid-State Light Sources Getting Smart, *Science*, 2005, **308**, 1274–1278.

2 P. Pust, P. J. Schmidt and W. Schnick, A revolution in lighting, *Nat. Mater.*, 2015, **14**, 454–458.

3 M. Zhao, H. X. Liao, M. S. Molokeev, Y. Y. Zhou, Q. Y. Zhang, Q. L. Liu and Z. G. Xia, Emerging ultranarrow-band cyan-emitting phosphor for white LEDs with enhanced color rendition, *Light: Sci. Appl.*, 2019, **8**, 38.

4 Y. Nanishi, The birth of the blue LED, *Nat. Photonics*, 2014, **8**, 884–886.

5 S. Pimputkar, J. S. Speck, S. P. DenBaars and S. Nakamura, Prospects for LED lighting, *Nat. Photonics*, 2009, **3**, 180–182.

6 N. C. George, K. A. Denault and R. Seshadri, Phosphors for Solid-State White Lighting, *Annu. Rev. Mater. Res.*, 2013, **43**, 481–501.

7 W. B. Im, N. George, J. Kurzman, S. Brinkley, A. Mikhailovsky, J. Hu, B. F. Chmelka, S. P. DenBaars and R. Seshadri, Efficient and Color-Tunable Oxyfluoride Solid Solution Phosphors for Solid-State White Lighting, *Adv. Mater.*, 2011, **23**, 2300–2305.

8 S. Adachi, Photoluminescence properties of Mn^{4+}-activated oxide phosphors for use in white-LED applications: A review, *J. Lumin.*, 2018, **202**, 263–281.

9 T. Rohmer, C. Lang, C. Bongards, K. B. S. S. Gupta, J. Neugebauer, J. Hughes, W. Gärtner and J. Matysik, Phytochrome as Molecular Machine: Revealing Chromophore Action during the Pfr → Pr Photoconversion by Magic-Angle Spinning NMR Spectroscopy, *J. Am. Chem. Soc.*, 2010, **132**, 4431–4437.

10 Z. Zhou, J. Zheng, R. Shi, N. Zhang, J. Chen, R. Zhang, H. Suo, E. M. Goldys and C. Guo, Ab Initio Site Occupancy and Far-Red Emission of Mn^{4+} in Cubic-Phase La$(MgTi)_{1/2}O_3$ for Plant Cultivation, *ACS Appl. Mater. Interfaces*, 2017, **9**, 6177–6185.

11 M. H. Du, Chemical trends of Mn^{4+} emission in solids, *J. Mater. Chem. C*, 2014, **2**, 2475–2481.

12 N. Mega, H. Tetsuo, H. Byungchul, O. Atsushi and O. Kazuyoshi, Study of multiplet structures of Mn^{4+} activated in fluoride crystals, *J. Lumin.*, 2016, **169**, 594–600.

13 Q. Y. Wu, C. X. Liao, J. Q. Pan, X. Y. Ye, W. X. You and L. B. Xia, HF-free molten salt route for synthesis of highly efficient and water-resistant K_2SiF_6: Mn^{4+} for warm white LED, *J. Am. Ceram. Soc.*, 2020, **103**, 6901–6912.

14 C. Stoll, J. Bandemehr, F. Kraus, M. Seibald, D. Baumann, M. J. Schmidberger and H. Huppertz, HF-Free, Synthesis of $Li_2SiF_6:Mn^{4+}$: A Red-Emitting Phosphor, *Inorg. Chem.*, 2019, **58**, 5518–5523.

15 H. D. Nguyen, C. C. Lin, M. H. Fang and R. S. Liu, Synthesis of $Na_2SiF_6:Mn^{4+}$ red phosphors for white LED applications by co-precipitation, *J. Mater. Chem. C*, 2014, **2**, 10268–10272.

16 E. H. Song, Y. Y. Zhou, X. B. Yang, Z. F. Liao, W. R. Zhao, T. T. Deng, L. Y. Wang, Y. Y. Ma, S. Ye and Q. Y. Zhang, Highly Efficient and Stable Narrow-Band Red Phosphor $Cs_2SiF_6:Mn^{4+}$ for High-Power Warm White LED Applications, *ACS Photonics*, 2017, **4**, 2556–2565.

17 M. H. Fang, H. D. Nguyen, C. C. Lin and R.-S. Liu, Preparation of a novel red $Rb_2SiF_6:Mn^{4+}$ phosphor with high thermal stability through a simple one-step approach, *J. Mater. Chem. C*, 2015, **3**, 7277–7280.

18 F. Hong, G. Pang, L. J. Diao, Z. D. Fu, G. X. Liu, X. T. Dong, W. S. Yu and J. X. Wang, Local structure modulation of Mn^{4+}-doped $Na_2Si_{1-y}Ge_yF_6$ red phosphors for enhancement of emission intensity, moisture resistance, thermal stability and application in warm pc-WLEDs, *Dalton Trans.*, 2020, **49**, 13805–13817.

This journal is © the Partner Organisations 2023

Inorg. Chem. Front., 2023, **10**, 2776–2787 | 2785

19 Q. Z. Dong, C. J. Guo, L. He, X. F. Lu and J. B. Yin, Improving the moisture resistance and luminescent properties of K_2TiF_6:Mn^{4+} by coating with CaF_2, *Mater. Res. Bull.*, 2019, **115**, 98–104.

20 Y. M. Liu, T. M. Wang, Z. R. Tan, J. M. Meng, W. J. Huang, Y. H. Huang, S. Liao and H. X. Zhang, Novel emission bands of Na_2TiF_6:Mn^{4+} phosphors induced by the cation exchange method, *Ceram. Int.*, 2019, **45**, 6243–6249.

21 L. Y. Wang, E. H. Song, Y. Y. Zhou, T. T. Deng, S. Ye and Q. Y. Zhang, An efficient and stable narrow band Mn^{4+}-activated fluorotitanate red phosphor Rb_2TiF_6:Mn^{4+} for warm white LED applications, *J. Mater. Chem. C*, 2018, **6**, 8670–8678.

22 F. Hong, L. Yang, H. P. Xu, Z. Y. Chen, Q. X. Liu, G. X. Liu, X. T. Dong and W. S. Yu, A red-emitting Mn^{4+} activated phosphor with controlled morphology and two-dimensional luminescence nanofiber film: Synthesis and application for high-performance warm white light-emitting diodes (WLEDs), *J. Alloys Compd.*, 2019, **808**, 151551.

23 T. C. Lang, T. Han, S. Q. Fang, J. Y. Wang, S. X. Cao, L. L. Peng, B. T. Liu, V. I. Korepanov and A. N. Yakovlev, Improved phase stability of the metastable K_2GeF_6:Mn^{4+} phosphors with high thermal stability and water-proof property by cation substitution, *Chem. Eng. J.*, 2019, **280**, 122429.

24 D. Li, Y. X. Pan, Y. Lin, L. J. Zhang, A. Y. Wang and J. Lin, Comparative investigation on solvent-related morphology and luminescence properties of a novel red phosphor $NaRbSnF_6$: Mn^{4+} for WLEDs application, *J. Lumin.*, 2020, **228**, 117577.

25 N. Ma, W. Li, B. Devakumar, S. Y. Wang, L. L. Sun, Z. J. Zhang and X. Y. Huang, Bright red luminescence from Mn^{4+} ions doped Sr_2LuTaO_6 double-perovskite phosphors, *J. Lumin.*, 2021, **233**, 117901.

26 G. C. Xing, Y. X. Feng, M. Pan, Y. Wei, G. G. Li, P. P. Dang, S. S. Liang, M. S. Molokeev, Z. Y. Cheng and J. Lin, Photoluminescence tuning in a novel Bi^{3+}/Mn^{4+} co-doped La_2ATiO_6:(A = Mg, Zn) double perovskite structure: phase transition and energy transfer, *J. Mater. Chem. C*, 2018, **6**, 13136–13147.

27 G. Li, X. Shi, X. Lu, Q. Mao, L. Pei, Y. Zhu, M. Liu, L. Chu and J. Zhang, Local Structure Modulation-Induced Highly Efficient Red-Emitting $Ba_2Gd_{1-x}Y_xNbO_6$:Mn^{4+} Phosphors for Warm WLEDs, *Inorg. Chem.*, 2021, **60**, 17398–17406.

28 D. Y. Huang, P. P. Dang, H. Z. Lian, Q. G. Zeng and J. Lin, Luminescence and Energy-Transfer Properties in Bi^{3+}/Mn^{4+}-Codoped Ba_2GdNbO_6 Double-Perovskite Phosphors for White-Light-Emitting Diodes, *Inorg. Chem.*, 2019, **58**, 15507–15519.

29 Z. F. Yang, L. L. Yang, C. J. Ji, D. H. Xu, C. Q. Zhang, O. X. Bu, X. Tan, X. Y. Yun and J. Y. Sun, Studies on luminescence properties of double perovskite deep red phosphor La_2ZnTiO_6:Mn^{4+} for indoor plant growth LED applications, *J. Alloys Compd.*, 2019, **802**, 628–635.

30 H. Chen, H. Lin, Q. M. Huang, F. Huang, J. Xu, B. Wang, Z. B. Lin, J. C. Zhou and Y. S. Wang, A novel double-perovskite Gd_2ZnTiO_6:Mn^{4+} red phosphor for UV-based w-LEDs: structure and luminescence properties, *J. Mater. Chem. C*, 2016, **4**, 2374–2381.

31 Y. F. Wang, F. Ding, J. Y. Wu, J. B. Ke, X. F. Wang and S. X. Lian, Site Preference-Driven Mn^{4+} Stabilization in Double Perovskite Phosphor Regulating Quantum Efficiency from Zero to Champion, *Inorg. Chem.*, 2022, **61**, 3631–3640.

32 K. Li, H. Z. Lian and R. Van Deun, A far-red-emitting $NaMgLaTeO_6$:Mn^{4+} phosphor with perovskite structure for indoor plant growth, *Dyes Pigm.*, 2019, **162**, 214–221.

33 J. Liang, B. Devakumar, L. L. Sun, Q. Sun, S. Y. Wang and X. Y. Huang, Mn^{4+}-activated $KLaMgWO_6$: A new high-efficiency far-red phosphor for indoor plant growth LEDs, *Ceram. Int.*, 2019, **45**, 4564–4569.

34 P. Q. Cai, C. L. Chen, J. Wang, S. L. Bi, S. I. Kim, Y. L. Huang and H. J. Seo, Optical Thermometry Based on Vibration Sidebands in Y_2MgTiO_6:Mn^{4+} Double Perovskite, *Inorg. Chem.*, 2018, **57**, 3073–3081.

35 A. A. Coelho, TOPAS and TOPAS-Academic: An Optimization Program Integrating Computer Algebra and Crystallographic Objects Written in C++, *J. Appl. Crystallogr.*, 2018, **51**, 210–218.

36 J. Li, J. M. Huang, P. F. Jiang, W. L. Gao, R. H. Cong and T. Yang, Complex crystal structure and photoluminescence of Bi^{3+}-doped and Bi^{3+}/Eu^{3+} co-doped $Ca_7Mg_2Ga_6O_{18}$, *Dalton Trans.*, 2021, **50**, 6848–6856.

37 R. D. Shannon, Revised Effective Ionic Radii and Systematic Studies of Interatomic Distances in Haildes and Chalcogenides, *Acta Crystallogr., Sect. A: Cryst. Phys., Diffr., Theor. Gen. Crystallogr.*, 1976, **32**, 751–767.

38 M. G. Brik and A. M. Srivastava, Electronic Energy Levels of the Mn^{4+} Ion in the Perovskite, $CaZrO_3$, *ECS J. Solid State Sci. Technol.*, 2013, **2**, R148–R152.

39 L. L. Sun, B. Devakumar, J. Liang, S. Y. Wang, Q. Sun and X. Y. Huang, Simultaneously enhanced far-red luminescence and thermal stability in $Ca_3Al_4ZnO_{10}$:Mn^{4+} phosphor via Mg^{2+} doping for plant growth lighting, *J. Alloys Compd.*, 2019, **785**, 312–319.

40 K. Seki, K. Uematsu, K. Toda and M. Sato, Novel Deep Red Emitting Phosphors $Ca_{14}Zn_6M_{10}O_{35}$:Mn^{4+} (M = Al^{3+} and Ga^{3+}), *Chem. Lett.*, 2014, **43**, 1213–1215.

41 L. Wang, L. Yuan, Y. D. Xu, R. L. Zhou, B. Y. Qu, N. Ding, M. Shi, B. Zhang, Y. Q. Chen, Y. Jiang and D. Wang, Luminescent properties of La_2LiTaO_6:Mn^{4+} and its application as red emission LEDs phosphor, *Appl. Phys. A: Mater. Sci. Process.*, 2014, **117**, 1777–1783.

42 Y. Takeda, H. Kato, M. Kobayashi, H. Kobayashi and M. Kakihana, Photoluminescence Properties of Mn^{4+}-activated Perovskite-type Titanates, La_2MTiO_6:Mn^{4+} (M = Mg and Zn), *Chem. Lett.*, 2015, **44**, 1541–1542.

43 S. Adachi, New Analysis Model for the Determination of Racah and Crystal-Field Splitting Parameters: Verification and Case Studies, *ECS J. Solid State Sci. Technol.*, 2020, **9**, 046004.

2786 | *Inorg. Chem. Front.*, 2023, **10**, 2776–2787

This journal is © the Partner Organisations 2023

44 S. Adachi, Mn^{4+} and Cr^{3+} ions in red and deep red-emitting phosphors: Spectroscopic analysis and Racah parameter determination, *J. Lumin.*, 2020, **223**, 117217.

45 S. Adachi, Crystal-field and Racah parameters of Mn^{4+} ion in red and deep red-emitting phosphors: Fluoride versus oxide phosphor, *J. Lumin.*, 2020, **218**, 116829.

46 M. G. Brik, S. J. Camardello and A. M. Srivastava, Influence of Covalency on the Mn^{4+} $^2E_g \rightarrow {}^4A_{2g}$ Emission Energy in Crystals, *ECS J. Solid State Sci. Technol.*, 2015, **4**, R39–R43.

47 J. X. Hu, T. H. Huang, Y.-P. Zhang, B. Lu, H. Q. Ye and H. P. Xia, Enhanced deep-red emission from Mn^{4+}/Mg^{2+} co-doped $CaGdAlO_4$ phosphors for plant cultivation, *Dalton Trans.*, 2019, **48**, 2455–2466.

48 X. Y. Huang and H. Guo, Finding a novel highly efficient Mn^{4+}-activated $Ca_3La_2W_2O_{12}$ far-red emitting phosphor with excellent responsiveness to phytochrome P-FR: Towards indoor plant cultivation application, *Dyes Pigm.*, 2018, **152**, 36–42.

49 L. L. Sun, B. Devakumar, J. Liang, B. Li, S. Y. Wang, Q. Sun and X. Y. Huang, Thermally stable $La_2LiSbO_6:Mn^{4+}$, Mg^{2+} far-red emitting phosphors with over 90% internal quantum efficiency for plant growth LEDs, *RSC Adv.*, 2018, **8**, 31835–31842.

50 J. Q. Chen, C. H. Yang, Y. B. Chen, J. He, Z. Q. Liu and J. Wang, Local Structure Modulation Induced Highly Efficient Far-Red Luminescence of $La_{1-x}Lu_xAlO_3:Mn^{4+}$ for Plant Cultivation, *Inorg. Chem.*, 2019, **58**, 8379–8387.

51 Y. B. Wu, Y. X. Zhuang, Y. Lv, K. B. Ruan and R. J. Xie, A high-performance non-rare-earth deep-red-emitting $Ca_{14-x}Sr_xZn_6Al_{10}O_{35}$: Mn^{4+} phosphor for high-power plant growth LEDs, *J. Alloys Compd.*, 2019, **781**, 702–709.

52 Y. Zhong, S. J. Gai, M. Xia, S. M. Gu, Y. L. Zhang, X. B. Wu, N. Zhou and Z. Zhou, Enhancing quantum efficiency and tuning photoluminescence properties in far-red-emitting phosphor $Ca_{14}Ga_{10}Zn_6O_{35}:Mn^{4+}$ based on chemical unit engineering, *Chem. Eng. J.*, 2019, **374**, 381–391.

53 N. Manson, G. Shah, B. Howes and C. Flint, $^4A_g \leftrightarrow {}^2E_g$ Transition of Mn^{4+} in Cs_2TiF_6: $MnF_6{}^{2-}$, *Mol. Phys.*, 1977, **34**, 1157–1174.

54 S. Adachi, Review—Temperature Dependence of Luminescence Intensity and Decay Time in Mn^{4+}-Activated Fluoride and Oxyfluoride Phosphors, *ECS J. Solid State Sci. Technol.*, 2021, **10**, 026002.

55 K. Li, J. R. Du, D. Poelman, D. Mara and R. V. Deun, Achieving Efficient Red-Emitting $Sr_2Ca_{1-\delta}Ln_\delta WO_6:Mn^{4+}$ (Ln = La, Gd, Y, Lu, $\delta = 0.10$) Phosphors with Extraordinary Luminescence Thermal Stability for Potential UV-LEDs Application via Facile Ion Substitution in Luminescence-Ignorable $Sr_2CaWO_6:Mn^{4+}$, *ACS Mater. Lett.*, 2020, **2**, 771–778.

56 S. N. Zhao, J. M. Xiang, M. H. Fang, C. H. Chen, M. K. Jin and N. M. Zhang, A novel high thermal stability $Ba_2CaWO_6:Mn^{4+}$ far-red emitting phosphor with double-perovskite structure for plant growth LEDs, *Opt. Mater.*, 2022, **124**, 112052.

57 Y. H. Kim, P. Arunkumar, B. Y. Kim, S. Unithrattil, E. Kim, S. H. Moon, J. Y. Hyun, K. H. Kim, D. Lee, J.-S. Lee and W. B. Im, A zero-thermal-quenching phosphor, *Nat. Mater.*, 2017, **16**, 543–550.

58 J. W. Qiao, L. X. Ning, M. S. Molokeev, Q. L. Liu and Z. G. Xia, Eu^{2+} Site Preferences in the Mixed Cation $K_2BaCa(PO_4)_2$ and Thermally Stable Luminescence, *J. Am. Chem. Soc.*, 2018, **140**, 9730–9736.

59 P. P. Dang, D. J. Liu, G. G. Li, A. A. Al Kheraif and J. Lin, Recent Advances in Bismuth Ion-Doped Phosphor Materials: Structure Design, Tunable Photoluminescence Properties, and Application in White LEDs, *Adv. Opt. Mater.*, 2020, **8**, 1901993.

60 L. Wu, S. J. Sun, Y. X. Bai, Z. G. Xia, L. W. Wu and H. M. Chen, Defect-Induced Self-Reduction and Anti-Thermal Quenching in $NaZn(PO_3)_3:Mn^{2+}$ Red Phosphor, *Adv. Opt. Mater.*, 2021, **9**, 2100870.

61 Y. X. Bai, S. J. Sun, L. W. Wu, T. G. Hu, L. R. Zheng, L. Wu, Y. F. Kong, Y. Zhang and J. J. Xu, Oxygen vacancy content drives self-reduction and anti-thermal quenching, *J. Mater. Chem. C*, 2022, **10**, 4317–4326.

62 T. Senden, R. J. A. van Dijk-Moes and A. Meijerink, Quenching of the red Mn^{4+} luminescence in Mn^{4+}-doped fluoride LED phosphors, *Light: Sci. Appl.*, 2018, **7**, 8.

63 S. Adachi, Review—Negative Thermal Quenching of Mn^{4+} Luminescence in Fluoride Phosphors: Effects of the $^4A_{2g} \rightarrow {}^4T_{2g}$ Excitation Transitions and Normal Thermal Quenching, *ECS J. Solid State Sci. Technol.*, 2022, **11**, 036001.

64 S. Adachi, Review—Temperature Dependence of Luminescence Intensity and Decay Time in Mn^{4+}-Activated Oxide Phosphors, *ECS J. Solid State Sci. Technol.*, 2022, **11**, 056003.

65 Y. Gao, Y. W. Zhao, P. F. Jiang, T. Wen, Y. G. Wang, R. H. Cong and T. Yang, Pressure-sensitive Ce^{3+} photo-luminescence in $LiCaY_5(BO_3)_6$: high internal quantum yields and energy transfer to Tb^{3+}, *J. Mater. Chem. C*, 2022, **10**, 17714–17722.

66 J. D. Barnett, S. Block and G. J. Piermarini, An Optical Fluorescence System for Quantitative Pressure Measurement in the Diamond–Anvil Cell, *Rev. Sci. Instrum.*, 1973, **44**, 1–9.

This journal is © the Partner Organisations 2023

Inorg. Chem. Front., 2023, **10**, 2776–2787 | **2787**